Article

A Failure Analysis of the Long-Term Overturning Stability of Concrete Continuous Single-Column Pier Bridges Considering Creep and Overloaded Vehicles

Yelu Wang [1,2], Jun Tian [3,*], Dong Zheng [4], Dayang Jing [5], Benzhen Cai [5] and Xiaofeng Liu [6]

1 School of Highway, Chang'an University, Xi'an 710064, China; 2017021032@chd.edu.cn
2 Key Laboratory of Bridge Detection Reinforcement Technology, Ministry of Communications, Xi'an 710064, China
3 Ordos Institute of Technology, Ordos 017000, China
4 Anhui Transport Consulting & Design Institute Co., Ltd., Hefei 230000, China
5 Jinan Urban Construction Group Co., Ltd., Jinan 250000, China
6 No.7 Geological Brigade, Shandong Provincial Bureau of Geology and Mineral Resources, Linyi 276000, China; liuxiaofeng396@163.com
* Correspondence: lele1008@oit.edu.cn

Abstract: Several single-column pier girder bridges have been involved in overturning accidents, resulting in significant economic losses and casualties, thus necessitating a risk assessment of the overturning stability. To date, the effect of structural degradation due to concrete creep on the long-term stability of bridges has not been demonstrated. In this study, a full-scale nonlinear analysis of the lateral overturning process of a collapsed concrete box girder based on the explicit dynamic finite element method (EFEM) was conducted to verify the reliability of the numerical method. An EFEM model incorporating concrete creep was developed to demonstrate the effect of structural degradation on the long-term stability of bridges. The synthesis overturning axis method (SOAM) was proposed to evaluate the long-term overturning stability of concrete continuous bridges, aiming to address the deficiencies in existing methods, particularly for curved bridges, and was compared with conventional methods. The results show that the variations in bearing reaction forces between curved and straight bridges under creep and self-weight are minimal, staying within 2%. An increase in the creep terminal coefficient results in the opposite trend in the ultimate vehicle weight of curved bridges and straight bridges, but fluctuations remain within 2%, indicating that long-term creep has a limited effect on the overall overturning stability. A failure analysis of 20 single-column pier bridges reveals significant differences in the ultimate vehicle weight between the rigid overturning axis method (ROAM) and folded overturning axis method (FOAM), with error ranges of −14.2% to 567.4% and −99.1% to −32.1%, respectively. The SOAM results have the smallest error range compared to those of the EFEM, with an error range of −38.8% to 33.9%. Despite these errors, the SOAM demonstrates a significant improvement in characterizing the trend and assessment accuracy of the overall overturning stability of single-column pier bridges.

Keywords: bridge engineering; single-column pier; collapse damage; overturning; creep; assessment method

1. Introduction

The construction of single-column piers generally needs small sites, which is beneficial to reducing environmental destruction, saving costs, and avoiding possible conflicts with underground architectures [1]. However, there have been many overturning instances of girder bridges with single-column piers in China and other locations as a result of overloaded vehicles, resulting in significant casualties and property damage [2–4]. The safety risks associated with these bridges have garnered widespread attention, making

it imperative to conduct overturning risk assessments for heavy-duty vehicles traversing single-column pier bridges [5].

Numerous scholars have extensively explored the bridge overturning issue through comprehensive approaches involving on-site investigation, theoretical analysis, numerical simulation, and testing. Fan [6] employed the qualitative data analysis package NVivo to analyze the system-wide failures and actions involved in the Yangmingtan bridge accident by collecting both texts and multimedia information from the web, newspapers, and videos. The results showed that the poor structural design, lack of regulation, and gaps between standards and practices were the primary causes of the accident. Peng [7] conducted forensic investigations on Chunhui Bridge and Hongfu Road Viaduct, and the results showed that the extrusion of the bridge bearings and the large eccentric compression failure of the columns under the overweight vehicles induced the progressive collapse. Peng [8] also reported that the mechanism of the overturning failure was a combination of a large rigid body rotation and a deformable body rotation. Liu [5] developed a mechanical model of a curved single-column pier bridge and derived analytical formulas for the bearing reaction force and torque, considering the bearing stiffness based on the force method principle. Lee [4] and Shi [9] developed a detailed solid or shell FE model of the accident bridge using the explicit dynamic finite element method (EFEM) to replicate the overturning damage process of the bridge due to vehicles. Wang [10] analyzed the two damage modes of the box girder (the slip and the bearing extrusions) and established the special force equilibrium system to determine whether or not the box girder was overturned through the energy method and variation principle. The most detailed solid model was developed by Song [11], which included the prestressing effect and diaphragms, and considered the actual configuration and dimensions of the pot rubber bearing, the material properties and boundary conditions of the rubber pads, and the contact properties between each part of the bearings. Xu [12] conducted in-situ overturning stability tests on a single-column pier bridge and verified the accuracy of the elastic model by comparing it with the field-measured data. While some meaningful progress has been achieved in the study of the overturning mechanism, it is important to note that bridge collapse is generally a very complex process involving various nonlinear geometric, material, and contact behaviors.

In terms of anti-overturning safety assessment methods, there are mainly the support reaction method (SRM), the overturning stability coefficient (OSC) method, and the EFEM [6,13]. In the past, engineers overly emphasized the strength of bridge structures and had an insufficient understanding of the bridge anti-overturning theory under overloaded vehicles. Simple measures to limit bearing disengagement were used to prevent overturning accidents [5]. However, the girder body exhibits nonlinear contact behavior during rotation, and the bridge overturning may not necessarily occur if a single bearing is detached. Therefore, it is not enough to judge the overturning of a bridge only through the separation of the bearings. The overall anti-overturning performance of the structure must be assessed in conjunction with the spatial characteristics of the girders. Subsequently, scholars began to adopt the OSC to evaluate bridges' anti-overturning stability [14]. The OSC is obtained by the ratio of the anti-overturning moment to the overturning moment relative to a certain overturning axis [15]. The OSCs vary depending on the overturning axis used, making it crucial to establish a suitable overturning axis before calculating the OSC. Wang [16] and Song [17] gave a method for determining the overturning axis based on the rigid rotation theory. Song [11] numerically analyzed the whole process of collapse of a continuous box girder bridge and found that the rotation axis gradually transited from the sectional centroid axis to a folded line through the supporting points of all the effective bearings; the analysis bridge exhibited a rigid-body rotation against the broken line near the ultimate overturning failure. Xiong [1] and Shi [15] found that an OSC based on rigid overturning axes overestimated the lateral stabilizing capacity of bridges without considering the second-order effects under large rotations. Li [18] has updated the OSC method by replacing the rigid axes with folded axes to account for the effects of deformed bodies during rotation. The updated OSC method has been incorporated into the MTPRC18

code and represents the most simplified method currently available. However, Zhou [19] and Song [11] highlighted several drawbacks of the updated OSC method: (1) it does not consider the anti-overturning effect of an individual support bearing during the girder rotation; (2) deploying the vehicle based on the most unfavorable state of the failed bearing may not ensure safety; (3) the direction of the moment vector on each fulcrum section of the curved girder varies throughout, making summing according to the scalar lack mechanical significance. The EFEM has been utilized to simulate structural collapse processes due to its ability to account for the discontinuous nonlinearity of structures and to capture transient behaviors during the collapse processes [9,20,21]. Despite its accuracy, the EFEM is time-consuming and not suitable for engineering application and promotion.

In terms of adverse loads in addition to overloaded vehicles that affect the overturning stability of bridges, temperature, foundation displacement, and earthquakes have also received extensive attention due to their destructive effects on bridges. Zhou [19] reviewed the effects and divergence of the above factors on bridges' overturning stability. Wang [22] analyzed the effect and mechanism of temperature on the overall overturning stability of single-column pier bridges using the EFEM, pointing out that the torsion induced by the gradient temperature exacerbates the overturning of curved bridges, while the upward deflection induced by the gradient temperature facilitates the separation of the girder and bearing. Deng [23] investigated the effect of a vehicle's centrifugal force and earthquakes on single-column pier bridges using the equivalent static load method and found that the centrifugal force and earthquakes will reduce the stability coefficient in an approximately linear manner. Peng [24] examined the effect of sound barriers on the stability of bridges using a beam element model and found that wind loads caused an increase in the rotation angle of the support. It is worth noting that the structural performance of the bridge degrades over time during the service process and the most significant problem is concrete creep. The creep can lead to additional deflection, cracking, prestress reduction, and internal force redistribution in bridges during the construction and service phases, and even affect the structure safety [25–28]. Some cases of bridge failure due to long-term creep have been reported, such as the Sanmenxia Yellow River Highway Bridge, which had a mid-span downward deflection of 22 cm after nine years of service [29]; the Koror-Babeldaob Bridge in the Republic of Palau also failed due to excessive time-varying deflection [30]. The additional deflection or internal force redistribution caused by concrete creep may decrease the stability of the bridge that prevents overturning. To date, the effect of creep on the lateral overturning stability of concrete bridges has not been demonstrated in detail.

In conclusion, the research on the overturning mechanism and calculation methods of concrete continuous bridges has yielded significant results. However, there are still some issues to address: (a) the effect of considering the performance degradation of concrete on the long-term overturning stability of bridges has not been adequately explored; (b) the updated OSC method is not able to analyze the long-term overturning stability of bridges with a small curvature radius. In this study, a collapsed three-span continuous concrete girder bridge was used as an example to simulate the entire overturning process under eccentric overloaded vehicles and to verify the reliability of the numerical method. Further, an EFEM numerical model considering concrete creep was developed to demonstrate its effect on the long-term anti-overturning stability of bridges. Finally, a new method was proposed to further update the OSC and improve the accuracy of the long-term overturning stability assessment of continuous girder bridges, especially for curved bridges. A comparison with the conventional method was made after considering the self-weight of the girders, vehicles, and concrete creep.

2. Failure Analysis of the Accident Bridge

2.1. Accident Bridge

A concrete continuous girder bridge measuring 22 + 35 + 25 m reportedly collapsed in China [31]. This unfortunate event led to three fatalities and two injuries, resulting in the direct economic loss of RMB 8.231 million and significant social repercussions. The bridge,

designed for a speed of 80 km/h, featured two lanes in each direction and a superstructure made of variable section prestressed concrete box girders. The bridge had two side piers with double bearings and two mid piers with single bearings. The bridge deck was 9.5 m wide, with a clearance of 5.2 m underneath. Notably, the side piers utilized one-way movable pot bearings with a 350 mm diameter, while the mid-pier bearings were two-way movable pot bearings with a diameter of 670 mm [32]. The bridge had not been reinforced before the accident. The detailed dimensions of the bridge are shown in Figure 1, and the cross-sectional parameters are plotted in Figure 2.
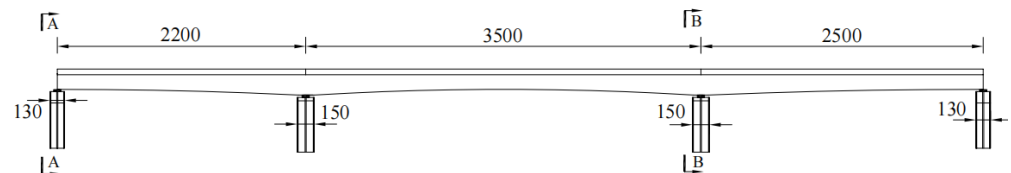
Figure 1. Elevation of the accident bridge (unit: cm).
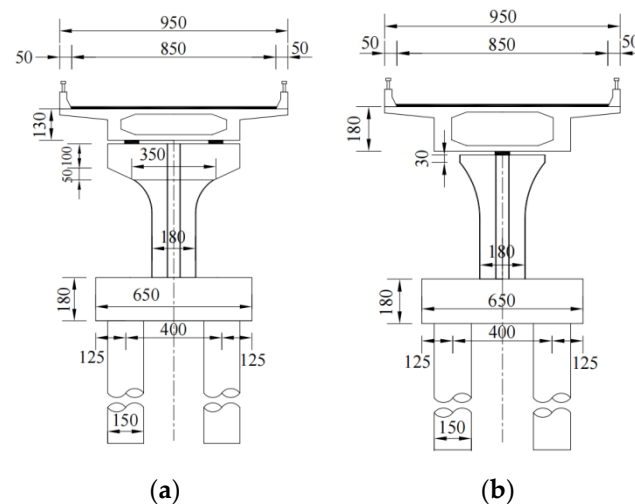
Figure 2. Cross-section of the accident bridge (unit: cm): (**a**) section A; and (**b**) section B.

2.2. Numerical Simulation

The bridge overturned during an incident involving two heavy tractor–trailer trucks, as detailed in the accident investigation report [31]. The front trailer was transporting seven coils of steel, totaling 160.5 tons, exceeding the permitted weight by 128.5 tons and overloading by 401.7%. Similarly, the rear trailer carried six coils of steel weighing 160.9 tons, surpassing the permitted weight by 131.9 tons and overloading by 454.7%. Additionally, at the time of the accident, two heavy trucks of 29 tons and 32 tons were present on the overturned bridge.

To investigate the behavior and mechanism during the collapse of the single-column-pier bridge, an FE model was meticulously created using the ANSYS/LS-DYNA program. In the FE model, the concrete girder was mainly made of a MAT1 material with elastic constitutive properties, while a MAT159 material was chosen for the possible contact areas between the girder and the bearings or piers. The rebar and beam elements were defined with a MAT3 material for the simulation. The maximum concrete aggregate size was 12 mm, and the Erode parameter was taken as 1.05. The modulus of elasticity of the rebars was 2.05×10^5 Mpa, and the standard value of tensile strength was 400 Mpa. The plastic strain at failure was set at 0.12. The bond between the concrete and rebar was established by a fluid–solid coupling connection using the keyword CONSTRAINED_LAGRANGE_IN_SOLID. The anti-collision guardrail and girder were constructed of C50 (with a prismatic compressive strength of 32.4 Mpa) concrete with a density of 2650 kg/m^3, an elastic modulus of 34.5 GPa, and a Poisson's ratio of 0.2. The piers were composed of C40 (with a prismatic

compressive strength of 26.8 Mpa) concrete with a density of 2650 kg/m^3, an elastic modulus of 32.5 GPa, and a Poisson's ratio of 0.2. The piers, bearings, and trucks were all made of a MAT1 elastomeric material. The truck tires and bearings were made of elastic rubber material. The diameter of the side-pier bearing was 350 mm and the height was 100 mm, while the diameter of the mid-pier bearing was 670 mm and the height was 160 mm. The bearing had an elastic modulus of 1.4 GPa, a Poisson's ratio of 0.499, and a density of 2000 kg/m^3. On the other hand, the tire's elastic modulus was 1.1 GPa, with a Poisson's ratio of 0.47 and a density of 1400 kg/m^3.

The bearings, girders, piers, wheels, and truck body were simulated by SOLID164 elements with grid sizes of 0.03 m, 0.1 m, 0.1 m, 0.1 m, 0.1 m, and 0.1 m. To avoid larger hourglass effects, the mesh size for the wheels was set to 0.1 m. Reinforcing bars were modeled using the beam elements, and a MAT3 material was chosen for the constitutive type. The bond between the concrete and the bars was linked by a fluid–solid coupling with the keyword *CONSTRAINED_LAGRANGE_IN_SOLID. The keyword for the contact between the vehicle and the girder was *CONTACT_AUTOMATIC_SURFACE_TO_SURFACE_ID, while the keywords for the contact between the girder and the bearing and the bearing and the abutment were *CONTACT_ERODING_SURFACE_TO_SURFACE_ID. The tangential contact relationship was modeled using a penalty function and the coefficient of friction was taken as 0.3. The bearing disengagement can be identified by determining if contact is maintained, specifically by checking if the contact force is zero. A more uniform hexahedral mesh was utilized to delineate the FE model and to avoid applying concentrated loads on the element nodes. The final control hourglass energy was lower than 10% of the total energy to ensure the calculation accuracy. A total of 352,169 nodes and 277,627 solid elements were established for the entire bridge. The established FE models of the bridge and vehicle are shown in Figure 3.
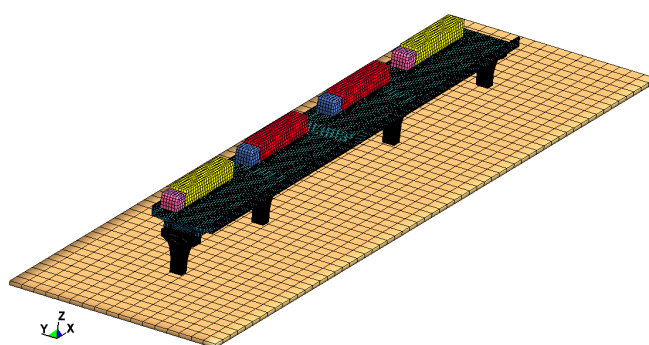
Figure 3. FE models of the accident bridge and vehicles.

The model's load comprised two main factors: the weight of the structure itself and of the trucks utilized. Gravity with an acceleration of 9.8 m/s^2 was utilized to determine the self-weight within the model. An arrangement of four trucks with six axles each was used for the vehicle loading, organized closely together. The weight distribution ratios for the initial six axles were as follows: 0.04, 0.19, 0.17, 0.21, 0.19, and 0.21. The total vehicle length measured 15 m, with axle spacings being 3.4 m, 0.9 m, 4.6 m, 1.6 m, and 1.6 m. Figure 4 displays the precise vehicle location, positioned 0.5 m from the edge of the curb. To ensure precision in the calculations and to avoid complications in convergence, as well as structural oscillations, gravitational force was gradually administered to the structure between a timespan of 0 s and 5 s. The bridge's quasi-static impact incorporated the implementation of substantial damping, where the damping coefficient equaled double the angular frequency of the bridge. During the simulation process, firm control over the model was dictated by the *CONTROL_HOURGLASS keyword, with the option of rigid hourglass control activated, holding a coefficient of 0.04. Mass scaling was effectively handled through the usage of the *CONTROL_TIMESTEP keyword being assigned a

negative value, guaranteeing that the proportion of added mass to the energy within the model was maintained under 5%.
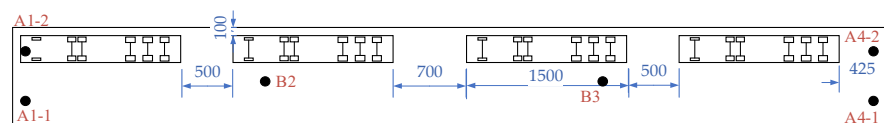
Figure 4. Plan layout of the accident bridge (unit: cm).

2.3. Overturning Process and Failure Characteristics

The analysis of vehicles crushing bridges was conducted. Some of the critical responses of the bridge were captured, such as the bearing reactions, girder displacements, and girder rotation angles. Figure 5a,b show the variation of the bearing reaction force of the bridge over time. At 13 s, the vertical reaction forces of bearings A1-2, A2, and B3 decrease significantly, while the horizontal forces of bearings B2 and B3 also decrease. In contrast, the horizontal forces of bearings A1-2 and A4-2 increase. Due to the horizontal force exerted by the vehicles being greater than the friction force between the bearing and the girder, the girder body slips. This slip causes a brief moment of weightlessness in the bridge, leading to a decrease in the vertical reaction force and horizontal force of the mid-pier bearing, while the side-pier bearing must bear a larger horizontal force to resist the girder body from sliding. During the bridge overturning, the vertical displacements on the non-overturned side of the girder are in the opposite direction to that of the overturned side and both of them increase gradually, as shown in Figure 5c. In Figure 5d, the rotation angles of each girder cross-section exhibit similar trends and magnitudes, all of which develop in an "S" shape, with a maximum difference of 0.12°. Figure 6 illustrates the process of the bridge overturning. During the rotation of the bridge, the vehicle slid 0.48 m transversely along the bridge and the tires contacted the underside of the guardrail. In combination with Figures 5 and 6, it can be seen that the accident vehicles were driving on one side of the bridge, leading to significant deformation and rotation of the box girder. As the girder rotates 5.8°, the horizontal force on the bearing surpasses the contact friction, causing the girder to slip. This results in the pier cap being cut and partially damaged, ultimately leading to the girder slipping off the bridge. Figure 7 shows the site wreckage of the bridge and the simulation results with the EFEM. The collapse posture of the girder aligns with the on-site wreckage, and the collapse process observed is consistent with the description provided in reference [32], thus validating the reliability of the numerical simulation.

Peng [7] pointed out that the sliding of the box girder, the bearing extrusion, or the eccentric compression failure of the piers may occur first during the rotation process of the box girder, and the overall overturning of the box girder is the upper limit of the anti-overturning capacity of single-column pier bridges. Therefore, the following assumptions were made during the overturning process: (1) the girders, bearings, and piers were in an elastic state and no strength damage occurred; (2) no interface slip occurred between the girder and bearings, bearings and piers, and vehicle and bridge deck. By adjusting the friction coefficient of the contact between the girder and the bearing to 10 and canceling the contact between the pier cap and the girder, the overall overturning mode of the bridge can be achieved. The trucks' weights were consistently modified to monitor the vertical reaction force of the bearings and the condition of the girder. When a specific truck weight was reached, the combined weight of the trucks at the moment of the bridge's first overturning is known as the ultimate vehicle weight for the overall overturning.

The weight of the vehicles was constantly adjusted until the bridge overturned. Figure 8a shows the variation in the vertical reaction forces at each bridge bearing with the vehicle weights. As the vehicle weight increases, the vertical reaction forces of the bearings A1-2 and A4-2 gradually increase, while the reaction forces of the other bearings decrease and eventually drop to zero. The sequence in which the bearings detach from the girder is as follows: A1-1 and A4-1, B2, B3, and A1-2 and A4-2. When the bridge is solely supported by bearings A1-2 and A4-2, the vertical reaction force of these side-pier

bearings peaks, then sharply decreases until disengagement, ultimately leading to the bridge's overturning. Thus, the support system degenerating into two bearings can serve as a mechanical criterion for determining the overall overturning of a bridge. Figure 8b illustrates the relationship between the rotation angle of the girder and the vehicle weights. The rotation angle of the girder is 0.004 rad when the bearings A1-1 and 4-1 are disengaged. According to the MTPRC 2019 code for bearings [33], limiting the rotation angle of bearings or girders within 0.02 rad may not prevent the bearings from detaching but can prevent overall overturning. Due to the ultimate vehicle weight, the girder experiences significant rotational deformation, reaching a rotation angle of 1.29 rad. It is demonstrated that rigid rotation theory is not applicable, because the overturning of the girder does not occur for rotation angles smaller than this angle.
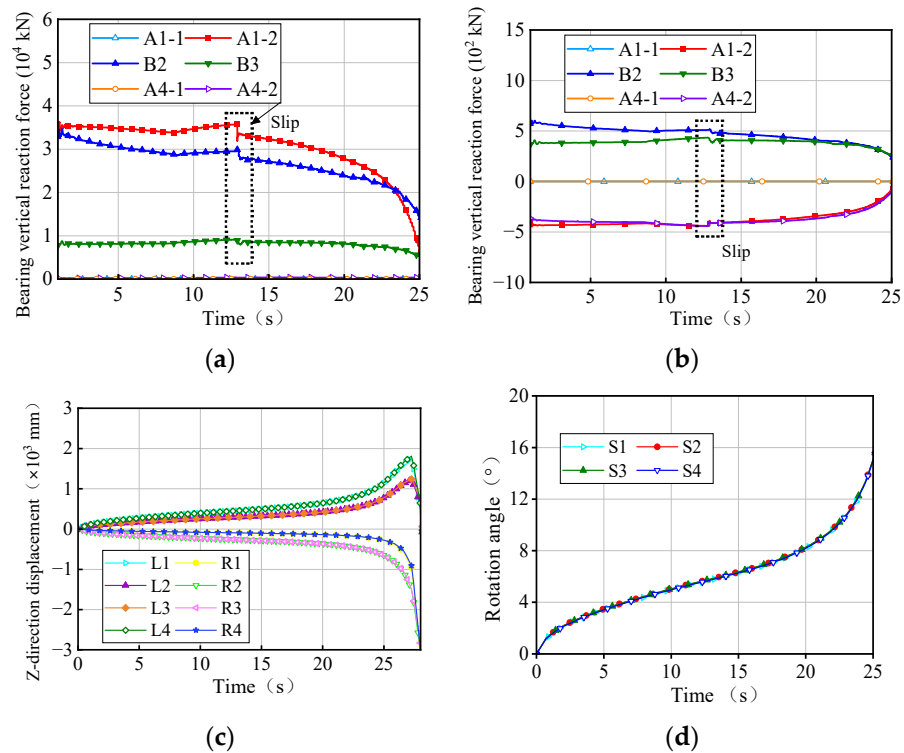
Figure 5. Overturning effects of the analysis bridge: (**a**) vertical reaction force of the bearings; (**b**) horizontal reaction force of the bearings; (**c**) z-direction displacement of the girder; and (**d**) rotation angle of the girder. Note that L_i and R_i denote the left and right sides of the girder section located above the ith pier position, respectively, while S_i represents the girder section above the ith pier.
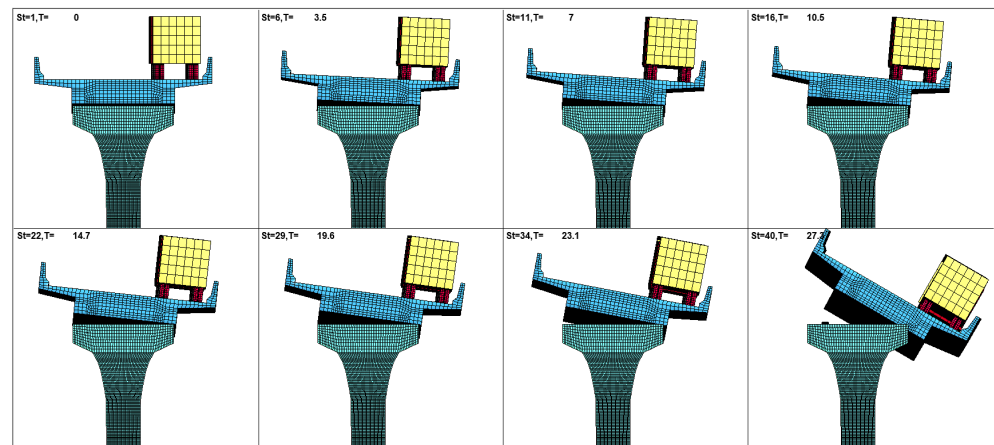
Figure 6. The overturning process of the accident bridge.
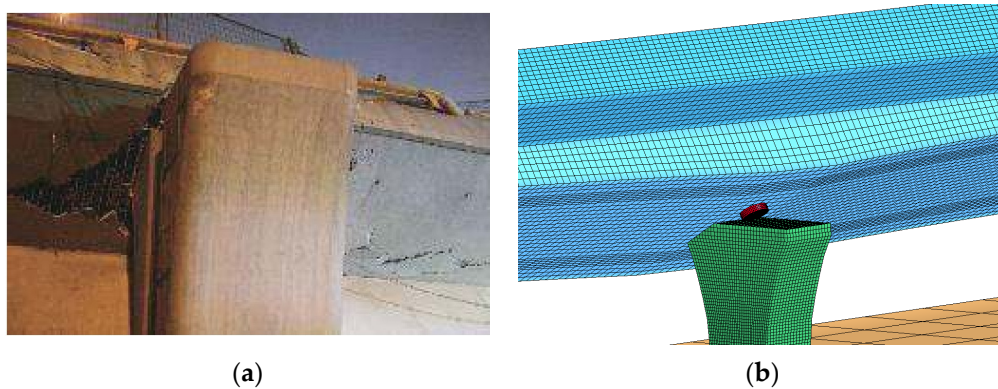
Figure 7. Comparison of bridge damage results: (**a**) destruction on-site; and (**b**) FEFM simulation results.
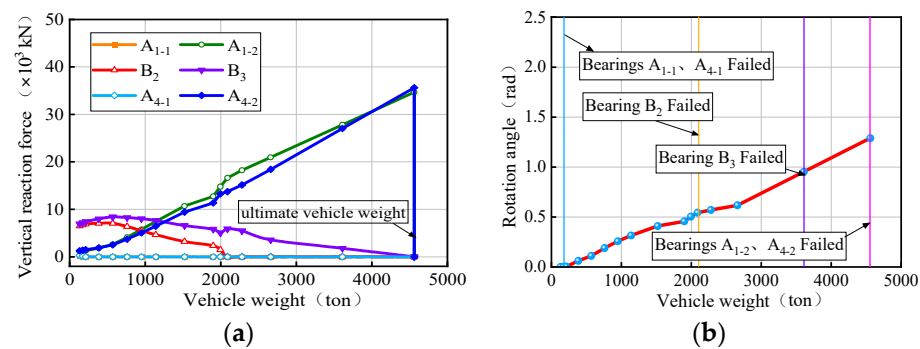
Figure 8. Overturning effects of the bridge under different trucks: (**a**) vertical reaction force of the bearings; and (**b**) rotation angle of the girder.

3. Verification of the Creep Model

3.1. Mathematical Model of Creep

In the past, most scholars believed that concrete creep or shrinkage was only a matter of material science [34]. However, the accumulation of test data and practical experience have contributed to a more profound understanding of the effects of shrinkage and creep on structures [35]. In practical structures, creep, shrinkage, and temperature strain are usually mixed. To obtain the creep strain, the temperature strain and shrinkage strain should be deducted from the measured strain. For a concrete member subjected to uniaxial constant stress $\sigma_0(t_0)$ at time t_0, the total strain $\varepsilon(t)$ at time τ can usually be decomposed into the following [35,36]:

$$
\begin{aligned}
\varepsilon(\tau) &= \varepsilon_i(t_0) + \varepsilon_c(\tau) + \varepsilon_s(\tau) + \varepsilon_T(\tau) \\
&= \varepsilon_\sigma(\tau) + \varepsilon_n(\tau)
\end{aligned}
\tag{1}
$$

where $\varepsilon_i(t_0)$ is the initial strain at the loading moment t_0; $\varepsilon_c(\tau)$ is the creep strain at the moment τ; $\varepsilon_s(\tau)$ is the shrinkage strain; $\varepsilon_T(\tau)$ is the temperature strain; $\varepsilon_\sigma(\tau)$ is the stress-generated strain; and $\varepsilon_n(\tau)$ is the non-stress-generated strain.

The concrete creep is usually described by the creep coefficient, and its variation pattern is shown in Figure 9. Currently, there are two different definitions of creep coefficient internationally: the CEB-FIP specification uses the instantaneous elastic strain of concrete at 28 days to define the creep coefficient (Equation (2)) [37], while the American ACI209 committee defines the creep coefficient as Equation (3).

$$
\varphi(\tau, t_0) = \frac{\varepsilon_c(\tau, t_0)}{\sigma(t_0)/E_{28}}
\tag{2}
$$

$$\varphi(\tau, t_0) = \frac{\varepsilon_c(\tau, t_0)}{\sigma(t_0)/E(t_0)} \tag{3}$$

where $\varepsilon_c(t, \tau)$ is the loading at time t_0 and the creep strain that occurs at time τ; $\sigma(t_0)$ is the loading stress at time t_0; E_{28} is the modulus of elasticity at 28 days; and $E(t_0)$ is the elastic modulus at loading time t_0.
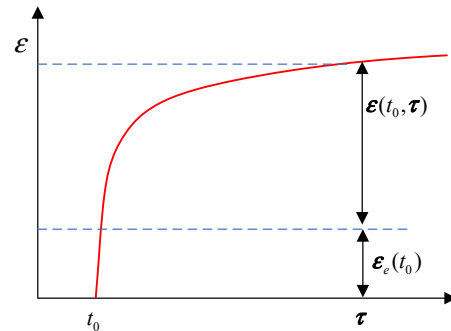
Figure 9. Schematic development curve of concrete creep.

The creep function $J(t_0, \tau)$ is the total strain generated at time t_0 after the uniaxial unit stress is applied to the concrete at time τ. For the above two definition methods of creep coefficient, the creep function can be expressed as follows [38]:

$$J(\tau, t_0) = \frac{1}{E(t_0)} + \frac{1}{E_{28}}\varphi(\tau, t_0) \tag{4}$$

$$J(\tau, t_0) = \frac{1}{E(t_0)}(1 + \varphi(\tau, t_0)) \tag{5}$$

The creep rate, on the other hand, is the creep strain produced by unit stress, and its expression is shown below:

$$C(t_0, t) = \frac{\varepsilon_c(\tau, t_0)}{\sigma(t_0)} = \frac{\varphi(\tau, t_0)}{E(t_0)} \tag{6}$$

Presently, there are two typical types of mathematical models for creep coefficients, one of which expresses the creep coefficient as the sum of several different subsections, while the other expresses the creep coefficient as the product of the coefficients of the creep-influencing factors. For example, the CEB-FIP 78 code [39] adopts the former creep coefficient expression:

$$\varphi(\tau, t_0) = \beta_a(t_0) + \varphi_d(\tau, t_0) + \varphi_r(\tau, t_0) \tag{7}$$

where $\beta_a(t_0)$ is the irrecoverable deformation coefficient-generated initial time of loading; $\varphi_d(\tau, t_0)$ is the recoverable elastic deformation coefficient; and $\varphi_r(\tau, t_0)$ is the irrecoverable rheology coefficient.

The creep coefficient expression of the CEB-FIP 90 [40] specification was revised to the coefficient product form [37]:

$$\varphi(\tau, t_0) = \varphi_0 \beta_c(\tau, t_0) = \Phi_{RH} B_{fcm} \beta(t_0) \beta_c(\tau, t_0) \tag{8}$$

where φ_0 is the nominal creep coefficient; Φ_{RH} is the correction coefficient for the environmental relative humidity; β_{fcm} is the correction coefficient for the concrete strength; $\beta(t_0)$ is the correction coefficient for the loading age; and $\beta_c(\tau, t_0)$ is the coefficient for the time of the creep process.

The creep of concrete increases monotonically with the loading time, but the increase rate gradually decreases. Assuming that the creep coefficient has a limit, it can be expressed as an exponential or a hyperbolic function [38]. When it is assumed that there is no limit to the creep coefficient, the form of a power or logarithmic function is usually used. Creep in concrete structures is a very complex phenomenon in which various uncertainties exist concerning inherent material variations as well as modeling uncertainties [37]. Numerous theoretical and experimental studies have been conducted in various creep prediction models [41,42]. In this study, a simple and efficient power function model (Equation (9)) is employed to consider the influence of creep. The effective stress–strain development curve of this creep model is depicted in Figure 10 [43].

$$\bar{\varepsilon}^c = A\bar{\sigma}^n \bar{t}^m \tag{9}$$

where A is the effective creep strain, m and n are constants, and $\bar{t}$ is the effective time.
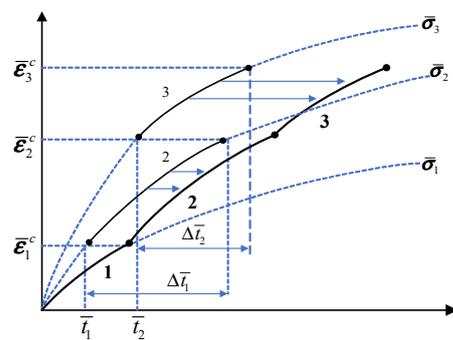
Figure 10. Development curve of the effective stress–strain. Note that the dashed lines represent the creep curves at constant $\bar{\sigma}$; the thin solid curve segments represent incremental trajectories along the creep curves; and the bold curve denotes the actual creep strain time history. More details of the parameters can be found in reference [43].

The effective stress $\bar{\sigma}$ is defined as follows:

$$\bar{\sigma} = \sqrt{\frac{3}{2}\sigma_{ij}\sigma_{ij}} \tag{10}$$

3.2. Validation of the Creep Model

To explore the creep pattern of prestressed concrete structures under variable loads, Zhao [44] conducted long-term experimental observation tests on model beams and obtained relatively credible results. In this study, the relevant parameters A, m, and n of the adopted mathematical model of creep were determined based on the experimental results of reference [44]. The experiment involved a box-shaped C50 prestressed concrete beam with a span of 3300 mm. At both ends of the beam, a 40 mm hole was reserved at the center of the cross-section to accommodate an unbonded prestressed rebar with a diameter of 32 mm. The dimensions of the experimental beam are shown in Figure 11, while the experimental scheme is shown in Figure 12.
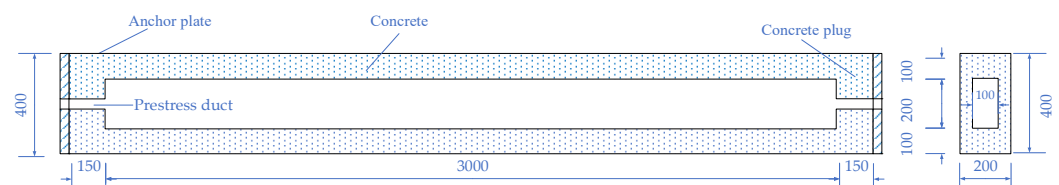
Figure 11. Experimental beam configuration (unit: mm).
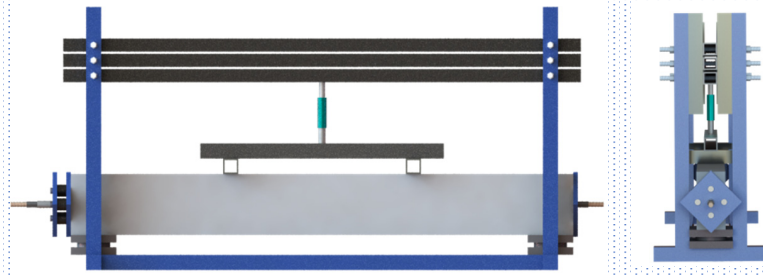
Figure 12. Experimental scheme.

The FE model of the experimental beam considering creep was established using ANSYS/LS-DYNA. The rebar and concrete were modeled using a decoupled approach. The beam was constructed with C50 (with a prismatic compressive strength of 32.4 Mpa) concrete with a density of 2650 kg/m^3, an elastic modulus of 34.5 GPa, and a Poisson's ratio of 0.2. The modulus of elasticity of the rebars was 2.05×10^5 Mpa, and the standard value of tensile strength was 400 Mpa. The modulus of elasticity of the prestressed rebar was 2.0×10^5 Mpa and the standard value of tensile strength was 930 Mpa. The concrete and rebar were simulated by Solid164 and Beam161 elements, respectively. The mesh size of the beams and rebars was 30 mm, while the mesh of the beam bottom pads was set to 20 mm. The entire model had a total of 8640 solid elements and 1176 beam elements. The bearing and beam adopted automatic surface contact with the keyword *CONTACT_AUTOMATIC_SURFACE_TO_SURFACE, and the friction coefficient was set to 0.3. The concrete was made of *MAT_UNIFIED_CREEP material that could be taken into account for the creep effect. The material parameters *A*, *m*, and *n* determined the developmental characteristics of the concrete creep. The entire FE model of the experimental beam is shown in Figure 13.

(**a**)

(**b**)
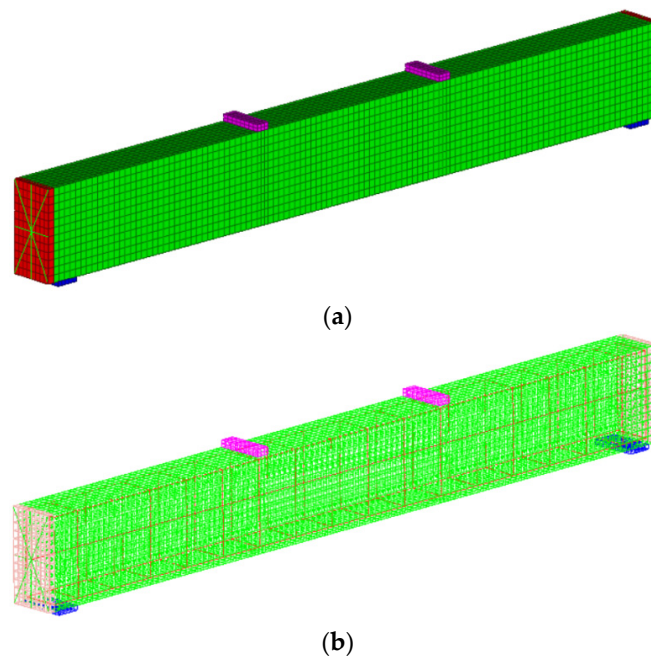
Figure 13. FE model of experimental beam: (**a**) concrete elements; and (**b**) coupling of rebar and concrete elements.

The fitting creep curve was obtained from the experimental results, as shown in Figure 14. The values of parameters *A*, *m*, and *n* were finally determined to be 2.21×10^{-6}, 1.36, and 0.43, respectively. By adding the above parameters to the material keywords, the fitted creep rate curves and total force strains of the experimental beams under incremental loads were ultimately achieved, as depicted in Figure 14.
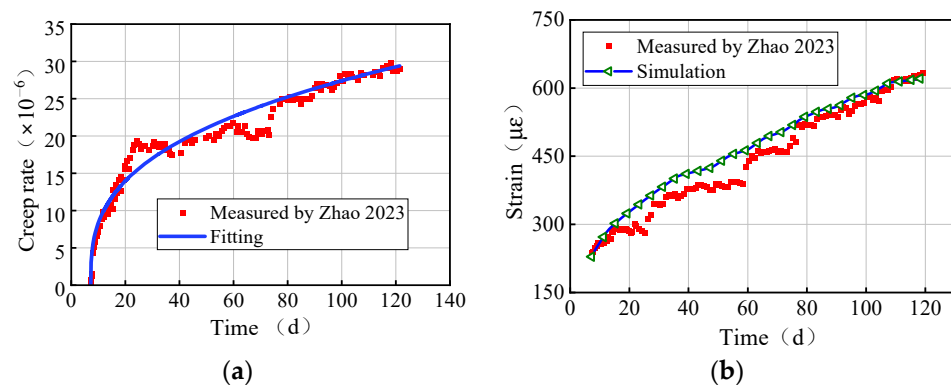
Figure 14. Comparison of measured in reference [44] and fitted results: (**a**) creep rate of the concrete roof plate; and (**b**) total force strain.

From the above figures, the calculated total strain aligns with the measured data trend, showing a gradual increase in forced strain over time with a decreasing slope, indicating a good simulation effect. This suggests that the creep material model can be further employed in the analysis of vehicle-induced bridge overturning.

4. Overturning Effects Induced by Creep

4.1. Bridge Categories

During the overall overturning process of the single-column pier bridge, the boundary conditions of the bridge continue to change, and each support fails one after another. Once the number of effective bearings is less than three, the bridge will suffer overall overturning. Previous studies have indicated that straight bridges and curved bridges exhibit different overturning characteristics [3,9,45]. According to the location of the last failed bearings, the distinguishing characteristics of the two types of bridges are as follows: the last two failed bearings of the curved bridge are the mid-pier bearings located on the outermost overturning side, providing effective torsional support (Figure 15a); whereas for the straight bridge, the last two bearings of the straight bridge to fail are the side-pier bearings on the overturning side, which serve as effective anti-torsional supports (Figure 15b).
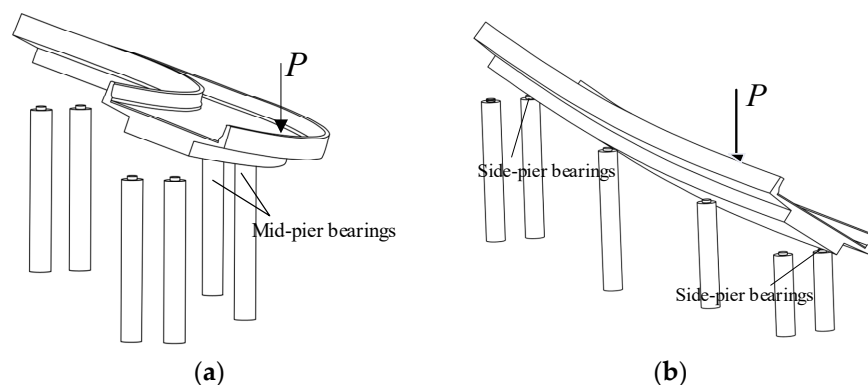
Figure 15. Schematic deformation of bridge overturning: (**a**) curved bridge; and (**b**) straight bridge. Note that *P* represents the eccentric vehicle load.

The critical curvature radius, as an essential parameter for distinguishing bridges, corresponds to the horizontal curvature radius of the bridge when the line connecting the bearings on the overturning side of all the piers becomes a straight line (Figure 16). Bridges with a radius smaller than the critical radius are considered curved bridges, whereas those with a radius larger than the critical value are categorized as straight bridges. In this study, curvature is a factor with both curved and straight bridges.
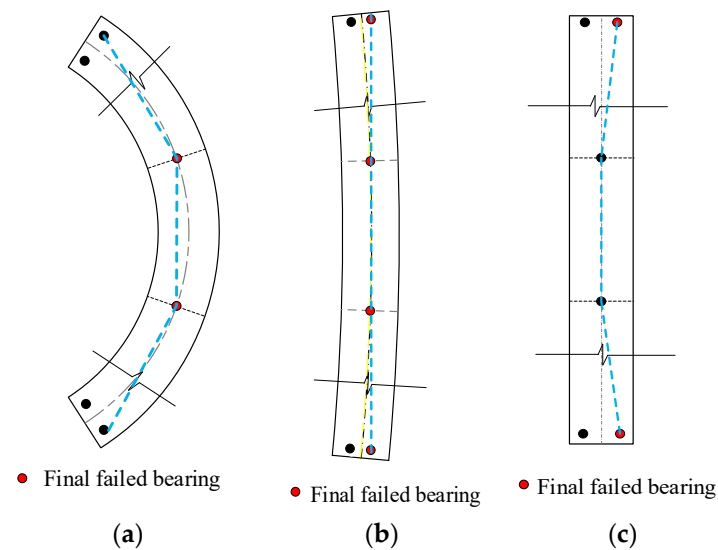
Figure 16. Bridge categories: (**a**) curved bridge; (**b**) critical bridge; and (**c**) straight bridge. Note: The blue dotted line represents the line connecting the bearings on the overturning side of all the piers.

Figure 17 illustrates the ultimate vehicle weights for bridges with a side-pier bearing spacing of 2.8 m. The critical bridges, identified by their critical curvature radius, are highlighted. The critical curvature radius gradually expands with the increase in the span number. When all the other parameters are held constant, the ultimate vehicle weight of the bridge decreases and then increases as the curvature radius varies, and extreme values can be observed. It is worth noting that the minimum value of the ultimate vehicle weight is associated with critical bridges. Overall, compared to curved bridges, straight bridges have a smaller ultimate vehicle weight, indicating relatively poor overall overturning stability.
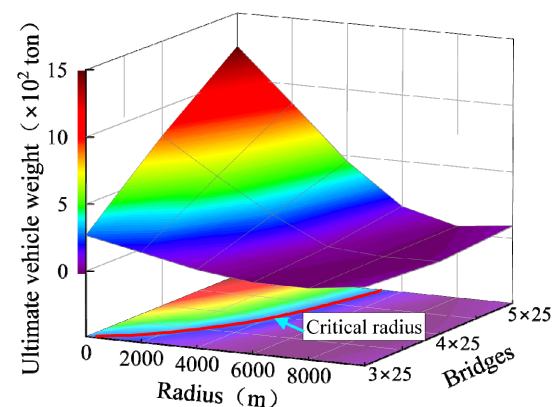
Figure 17. Ultimate vehicle weight for bridges.

4.2. Overturning Effect

Furthermore, the effect of creep on the overall overturning stability of single-column pier bridges was analyzed. A "pseudo-time" analysis was performed during the first 20 s to fully account for the effects of the terminal creep on the girder after 10 years. After 20 s, the effects of the creep were no longer accounted for. Parameter A was adjusted to 2.22×10^{-6}, 4.43×10^{-6}, 6.63×10^{-6}, and 8.84×10^{-6} to account for the creep terminal coefficients ψ of 1.25, 1.5, 1.75, and 2. The bridges with a curvature radius of 80 m and 10,000 m were classified as straight bridges and curved bridges, respectively. Additionally, three-span and five-span single-column pier bridges were also considered. The girder material remained consistent with the discussion in Section 3.1, while the materials for the other bridge components matched those detailed in Section 2.2. For the bearings, A represents the side-

pier bearing, while B represents the mid-pier bearing. Figure 18 presents the dimensions of the cross-section of the bridge. The modeling process for the entire bridge followed a similar approach to that outlined in Section 2.2. The vehicle location and number were determined based on the influence surface, which was used to obtain the most unfavorable effect of overturning through the fabric loads of the influence surface.
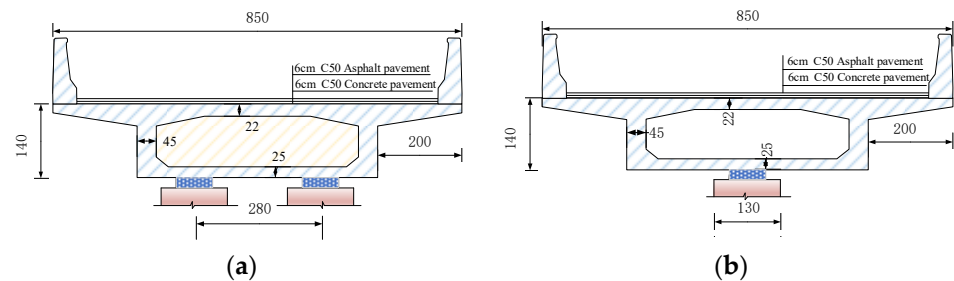
Figure 18. Girder cross-section (unit: cm): (**a**) girder section at side-pier location; and (**b**) girder cross-section at mid-pier location.

The bearing reactions of the four bridges subjected to creep and self-weight are presented in Figures 19 and 20. After considering the creep, the variation ranges of the vertical reaction forces for each bearing of the 3×25 m and 5×25 m curved bridges were -0.8% to 1.4% and -0.2% to 0.3%, respectively. Similarly, for the 3×25 m and 5×25 m straight bridges, the vertical reaction force variation ranges for each bearing were -0.8% to 1.4% and -0.2% to 0.3%, respectively. Overall, it can be observed that the changes in the bearing reaction forces due to creep are within 2% for both the curved and straight bridges.
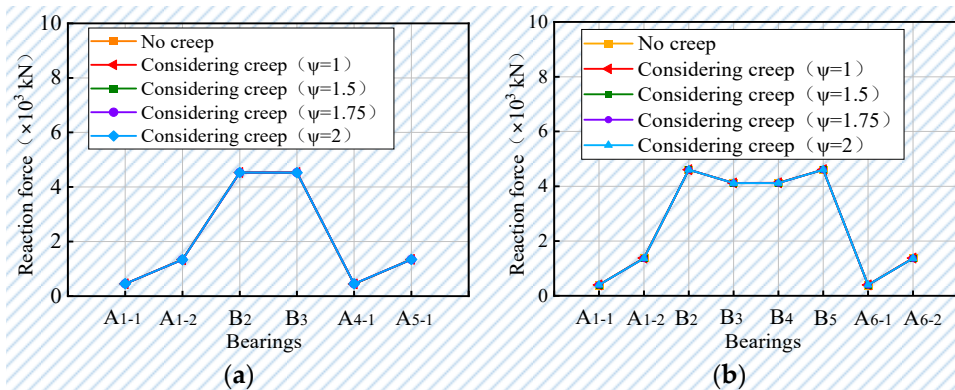
Figure 19. Bearing vertical reaction forces for the curved bridges: (**a**) 3×25 m bridges; and (**b**) 5×25 m bridges.
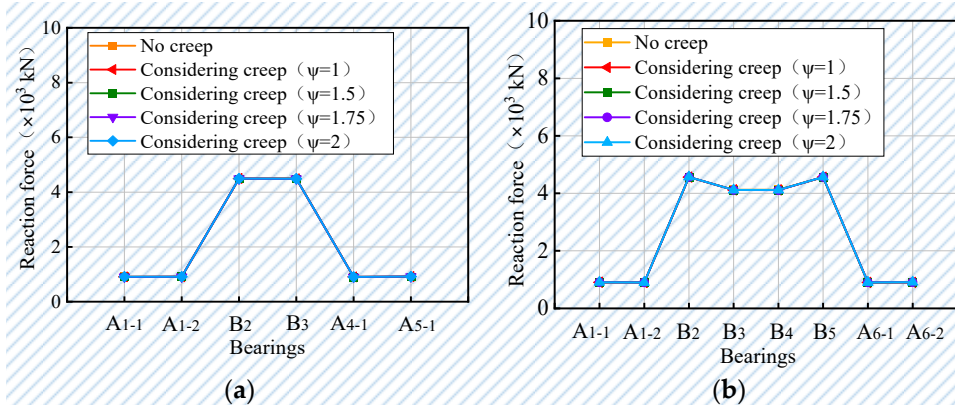
Figure 20. Bearing vertical reaction forces for the straight bridges: (**a**) 3×25 m bridges; and (**b**) 5×25 m bridges.

The failure analysis of vehicles collapsing a bridge was conducted by placing vehicles on a bridge for which creep had been considered. The degradation of the bridge into two bearing support systems could be used as a supplementary criterion for the overall overturning. Figures 21 and 22 show the ultimate vehicle weights obtained by the EFEM for the 3×25 m and 5×25 m bridges. For curved bridges, the ultimate vehicle weights gradually increase as the creep terminal coefficient increases. Specifically, when the creep terminal coefficient was 2, the ultimate vehicle weights of 3×25 m and 5×25 for the curved girder bridges increased by 0.1% and 0.2%, respectively. The ultimate vehicle weights for the straight bridges decrease gradually as the creep terminal coefficient increases. Specifically, when the creep terminal coefficient was 2, the ultimate vehicle weight of the 3×25 m and 5×25 m straight bridges were reduced by 1.6% and 1.1% respectively. Comprehensively, it can be seen that the variation of the ultimate vehicle weights of both curved and straight bridges caused by creep is within 2%. This indicates that the concrete creep has a limited effect on the long-term overall overturning stability of the single-column pier bridge compared to temperature and overloaded vehicles.
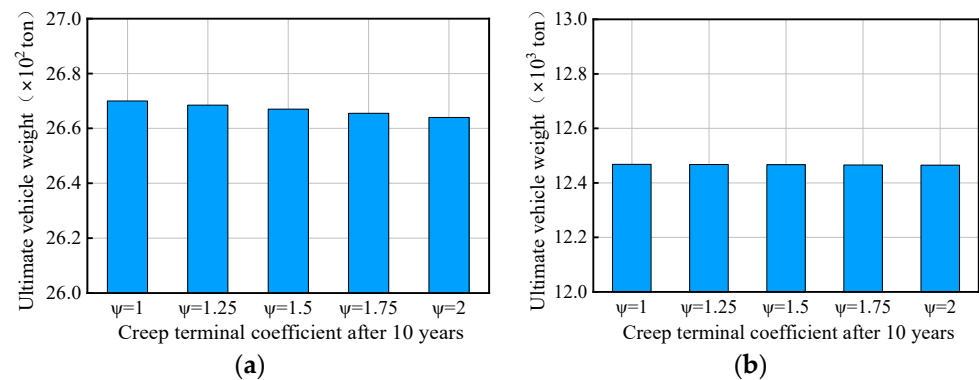
Figure 21. Ultimate vehicle weights of the overall overturning for the curved bridges: (**a**) 3×25 m bridges; and (**b**) 5×25 m bridges.
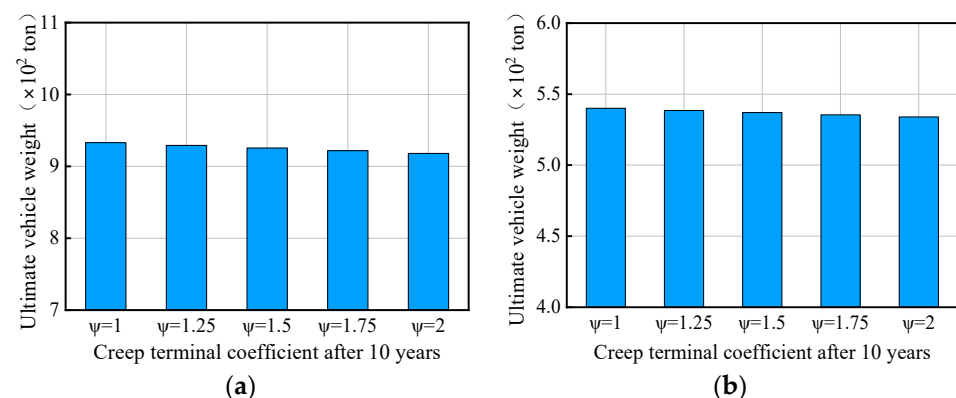
Figure 22. Ultimate vehicle weights of the overall overturning for the straight bridges: (**a**) 3×25 m bridges; and (**b**) 5×25 m bridges.

Since the overall overturning is the upper limit of the overturning capacity of a bridge and the influence of creep on the bearing reaction force and the ultimate vehicle weight is within 2%, it can be inferred that the influence of creep on all other failure modes of the bridge overturning is small, such as the girder sliding failure, bearing extrusion failure, and pier failure. Many scholars have proposed many creep models, and different mathematical models and different simulation software may cause calculation errors. Overall, concrete creep has little effect on the overturning stability of curved and straight bridges. It is not of practical significance to analyze the mechanism of bridge overturning caused by creep. In the design and maintenance stages of the bridge, a coefficient of 0.98 can be considered

to discount the overall overturning stability of the bridge, which will simplify the design process and improve efficiency.

5. Assessment of Overturning Stability

Many scholars have highlighted the lack of code information as a significant reason leading to the susceptibility of bridges to overturning accidents during their operation [13,17]. An accurate assessment method for the overturning stability of single-column pier bridges can help provide guidance for bridge design or maintenance and provide early warning of potential disasters.

Currently, measures to prevent the bridge from overturning collapse can be categorized into three aspects: (1) preventing the bearing from disengagement or limiting the bearing reaction force; (2) ensuring the girder or bearing angle does not exceed the limitation; (3) enabling an OSC of greater than 1, resulting in more surplus.

There are definite provisions on the bearing disengagement state in several specifications. The Chinese specification MTPRC 2004 requires that the bearing remain in compression under the basic combination of loads [45]. Both SIA 260 and EN 1990 specify that the design value of the destabilizing action should be less than or equal to the value of the stabilizing action [46]. Specifically, the AASHTO 2012 code [47] recommends that the support reaction force of a multi-directional movable bearing should be at least 20% of the vertical capacity of the bearing. The MTPRC 2018 code [48] mandates that bearings must remain in compression under the basic load combinations, while the MTPRC 2005 code [49] requires the minimum compressive stress of the bearing to be greater than 2 Mpa. The JRA 2012 code [50] considers twice the live load effect to be a factor in limiting the negative reaction force of the bearing. Simply limiting the bearing and girder rotation angles is insufficient. Following a series of bridge overturning accidents, the MTPRC 2018 code introduced additional calculation methods and a requirement for the OSC to assess the overturning stability of bridges. The OSC can be formulated in the following way [24,46]:

$$r_{qf} = \frac{M_b}{M_s} \quad (11)$$

where γ_{qf} is the lateral OSC of the bridge; and M_b and M_s are the stabilizing and overturning moments, respectively.

The results of the OSC depend on the choice of the overturning axis. Previous studies have demonstrated that neither a rigid overturning axis nor a flexible overturning axis can characterize the overturning deformation of a bridge. Observing the state of the overall overturning of curved and straight bridges in Figure 15 and considering the effect of long-term creep, a synthesis overturning axis and associated synthesis overturning axis method (SOAM) were proposed to evaluate the overall overturning stability of bridges. The SOAM still utilizes the expression form of the OSC, with the major difference being the comprehensive overturning axis it relies on. Figures 23 and 24 illustrate the synthesis of the overturning axes for the circular bridge and the straight bridge, respectively. Table 1 provides a list of the relevant parameters for both curved and straight bridges.

$$\gamma_{qf} = \frac{\sum M_b}{\sum M_s} \phi_c \quad (12)$$

$$\sum M_b = \sum R_{Gi} l_i \quad (13)$$

$$\sum M_s = \sum R_{qi} l_i \quad (14)$$

where ϕ_c represents the long-term performance degradation factor, with a value of 0.98; R_{Gi} is the vertical reaction force of the ith bearing under gravity; l_i is the vertical distance of the ith bearing from the synthesis overturning axis; and R_{Gi} is the vertical reaction force of the ith support under a live load, which may be from vehicles, temperature, or a combination of both. The synthesis overturning axes are determined by Table 1.
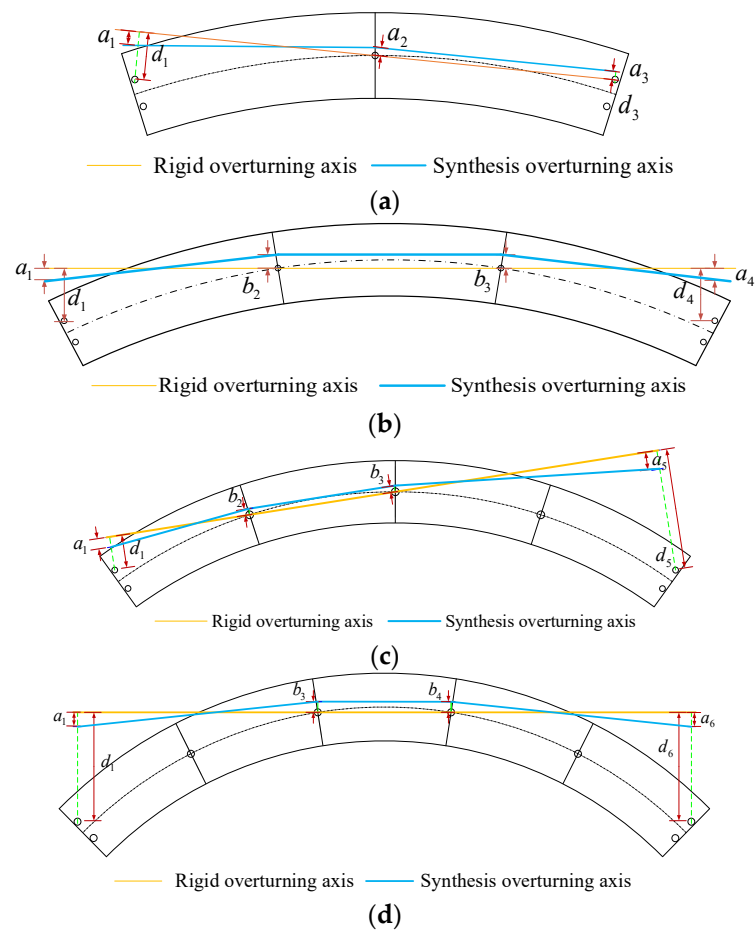
Figure 23. Synthesis overturning axes for the curved bridges: (**a**) two-span continuous bridge; (**b**) three-span continuous bridge; (**c**) four-span continuous bridge; and (**d**) five-span continuous bridge.
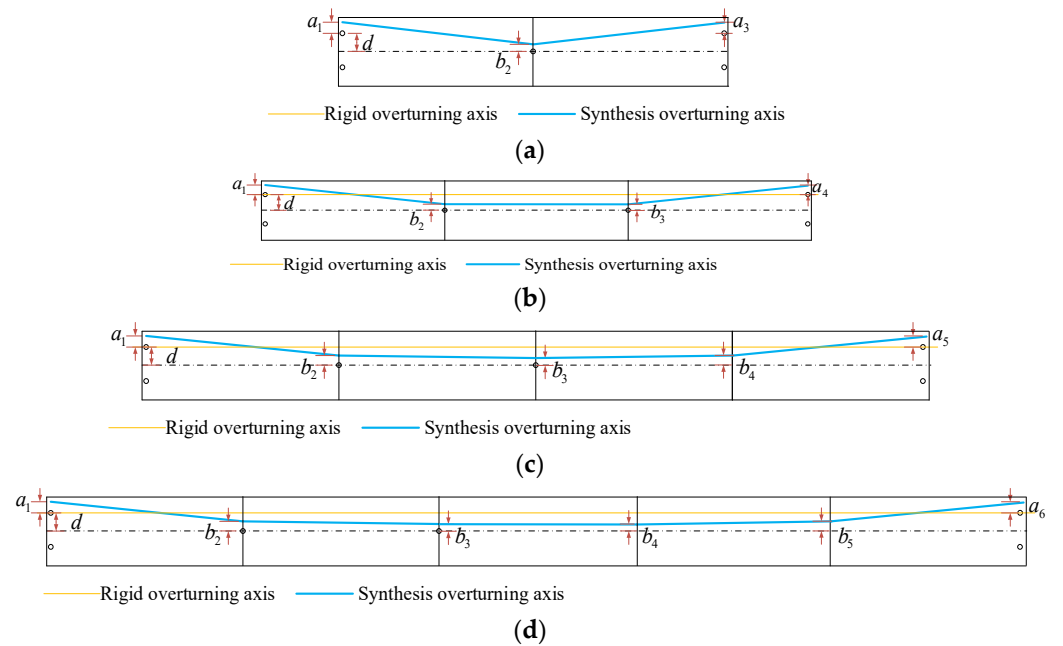
Figure 24. Synthesis overturning axes for the straight bridges: (**a**) two-span continuous bridge; (**b**) three-span continuous bridge; (**c**) four-span continuous bridge; and (**d**) five-span continuous bridge.

Table 1. Parameters of the synthesis overturning axis.

Bridge Type	Curved Bridge	Straight Bridge
Two-span continuous bridge	$a_1 = \frac{B}{2L}d_1$ $b_2 = b_3 = 0.5h_e$	$a_i = 0.5h_e$ $b_2 = 0.5d$
Three-span continuous bridge	$a_i = \frac{B}{2L}d_i$ $b_i = 0.5h_e$	$a_i = 0.5h_e$ $b_i = \frac{B}{L}d$
Four-span continuous bridge	$a_1 = \frac{B}{2L}d_1$ $a_5 = \frac{B}{2L}d_5$ $b_2 = b_3 = 0.5h_e$	$a_i = 0.5h_e$ $b_2 = \frac{B}{L}d$ $b_3 = b_4 = 0.5h_e$
Five-span continuous bridge	$a_i = \frac{B}{L}d_i$ $b_3 = b_4 = 0.5h_e$	$a_i = 0.5h_e$ $b_2 = b_5 = \frac{B}{L}d$ $b_3 = b_4 = 0.5h_e$

Note that B represents the width of the bridge; L is the maximum value of the left and right spans; a_i is the distance between the ith side-pier bearing and the synthesis overturning axis; b_i is the distance between the mid-pier bearing and the synthesis overturning axis; d_i is the distance between the mid-pier bearing and the rigid overturning axis; d is the distance from the side bearing to the central axis of the bridge; and h_e is the effective height of the bearing, which is 0.75 times the bearing height.

The method of evaluating the overturning performance of a bridge using the OSC with a rigid overturning axis is known as the rigid overturning axis method (ROAM). On the other hand, the method that employs the OSC with a fold overturning axis is referred to as the fold overturning axis method (FOAM). It should be noted that the FOAM and ROAM employ Equation (11) to calculate the stability coefficient, whereas the SOAM utilizes Equation (12). To compare the variability of the methods in the assessment of the overall overturning load capacity of bridges, overturning analyses were conducted on two types of bridges: curved bridges with a span of 80 m and straight bridges with a span of 10,000 m. These bridges were typical single-column pier bridges that had not been reinforced. The factors of the side-to-mid span ratio (STMR), span length, and span numbers were adjusted to cover wider bridges. The calculation parameters of the bridges are detailed in Tables 2 and 3. The form of bearing support, girder cross-section, and wheel load distribution were consistent with Section 2.2. The vehicle loads were distributed in the most unfavorable position according to the influence surface of the maximum overturning effect. The evaluation index of the bridge stability performance obtained by the EFEM was the ultimate vehicle weight, whereas the evaluation index obtained by the ROAM, FOAM, and SOAM was the OSC. To facilitate the comparison, the ultimate vehicle weight was used as the sole indicator of the bridge stability performance. Considering the effects of gravity, vehicles, and the long-term performance degradation caused by concrete creep, the ultimate vehicle weights for the ROAM, FOAM, and SOAM could be obtained by setting the OSC to 1. The ultimate vehicle weights calculated by the EFEM were more accurate due to the consideration of structural dimensions and nonlinearities, serving as a reference for the other methods.

Table 2. Parameters of the curved bridges.

Curvature Radius (Unit: m)	Bridge No.	Ratio of Side-Span to Mid-Span	Total Span Length (Unit: m)
	1	0.6	15 + 25 + 15
	2	0.8	20 + 25 + 20
	3	1	25 + 25 + 25
	4	1.2	30 + 25 + 30
	/	Single-span length (unit: m)	Total span length (unit: m)
	3	25	25 + 25 + 25
80	5	30	30 + 30 + 30
	6	35	35 + 35 + 35
	7	40	40 + 40 + 40
	/	Span number	Total span length (unit: m)
	8	2	25 + 25
	3	3	25 + 25 + 25
	9	4	25 + 25 + 25 + 25
	10	5	25 + 25 + 25 + 25 + 25

Table 3. Parameters of the straight bridges.

Curvature Radius (Unit: m)	Bridge No.	Ratio of Side-Span to Mid-Span	Total Span Length (Unit: m)
	1	0.6	15 + 25 + 15
	2	0.8	20 + 25 + 20
	3	1	25 + 25 + 25
	4	1.2	30 + 25 + 30
	/	Single-span length (unit: m)	Total span length (unit: m)
	3	25	25 + 25 + 25
	5	30	30 + 30 + 30
10,000	6	35	35 + 35 + 35
	7	40	40 + 40 + 40
	/	Span number	Total span length (unit: m)
	8	2	25 + 25
	3	3	25 + 25 + 25
	9	4	25 + 25 + 25 + 25
	10	5	25 + 25 + 25 + 25 + 25

Figure 25 presents the ultimate vehicle weights for bridge overturning obtained through various methods under the influence of the STMR. The EFEM results indicate that as the STMR increases, the ultimate vehicle weights for curved bridges gradually increase, while those for straight bridges decrease. This indicates that the increase in the STMR is beneficial to the stability of curved bridges and weakens the stability of straight bridges. In terms of trends, the ROAM shows a similar pattern to the EFEM when evaluating the anti-overturning performance of curved bridges. Similarly, the SOAM displays similar trends to the EFEM in both curved and straight bridges. However, the FOAM does not accurately represent the evolution pattern of the overall anti-overturning performance in both types of bridges. Furthermore, the ROAM is unable to accurately characterize the evolution law of the anti-overturning load-bearing capacity in straight bridges.
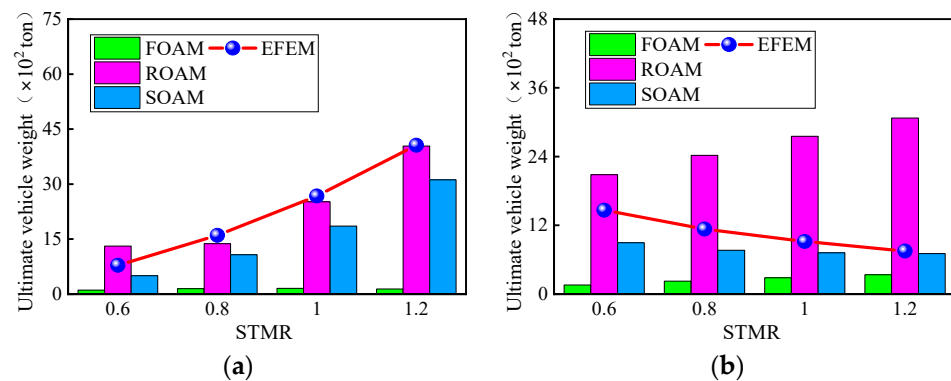
Figure 25. Ultimate vehicle weights for the bridges with various side-to-mid span ratios (STMR): (**a**) curved bridges; and (**b**) straight bridges.

In terms of accuracy, the SOAM exhibits the least error compared to the EFEM, ranging from −23.2% to −36.4%, followed by the ROAM with an error range of −14.3% to 66.4%. The ultimate vehicle weight calculated using the FOAM is only 3.3%, compared to 13.8% for the EFEM, which significantly underestimates the anti-overturning capacity of curved bridges. For straight bridges, the SOAM shows the least error with −6.1%, compared to −38.8% for the EFEM. The ultimate vehicle weights obtained by the FOAM are only 10.9%, compared to 44.8% for the EFEM, with errors ranging from −55.7% to −89.2%, which indicates that the method underestimated the overturning load capacity of straight bridges. On the other hand, the ultimate vehicle weight calculated using the ROAM is 1.4 to 4.1 times that of the EFEM, indicating an overestimation of the anti-overturning capacity of straight bridges.

Figure 26 shows the ultimate vehicle weight required for the overall overturning of bridges under varying span lengths, as determined by different methods. The EFEM results indicate that as the span length increases, the ultimate vehicle weight for curved bridges gradually increases, whereas, for straight bridges, it initially decreases before increasing. The increase in span length is advantageous for the stability of curved bridges, while its influence on straight bridges is more intricate. In analyzing the anti-overturning performance of curved bridges, the ROAM exhibits a pattern similar to the EFEM, while the SOAM demonstrates comparable trends to the EFEM in both curved and straight bridges. However, the FOAM does not effectively capture the overall evolution of anti-overturning performance on both bridge types. Additionally, the ROAM fails to accurately depict the evolution of anti-overturning load-bearing capacity of straight bridges.
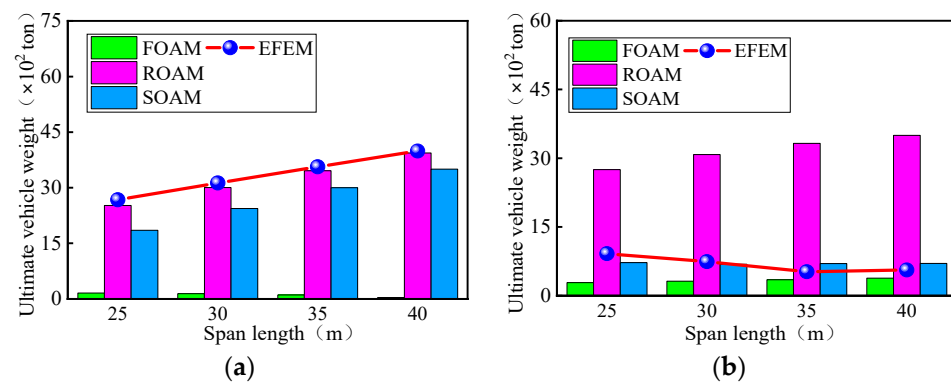
Figure 26. Ultimate vehicle weights for the bridges with various span lengths: (**a**) curved bridges; and (**b**) straight bridges.

In terms of accuracy, for the curved bridges, the ROAM exhibits the least error in comparison to the EFEM, ranging from −1.3% to −5.9%, followed by the SOAM with an error range of −12.3% to −30.8%. For the straight bridges, the errors of the SOAM compared with the EFEM are the minimum, ranging from −21.5% to 33.9%. The ultimate vehicle weight obtained by the FOAM is 31.1%, compared to 58.6% with the EFEM, indicating an underestimation of the anti-overturning capacity of straight bridges. On the other hand, the ultimate vehicle weight obtained by the ROAM is 3.0 to 6.4 times that of the EFEM, which overestimates the anti-overturning load-bearing capacity of straight bridges.

Figure 27 illustrates the ultimate vehicle weights for bridge overturning obtained by different methods under the influence of the span number. The EFEM results indicate that the ultimate vehicle weight for curved bridges gradually increases as the span number increases, while that for straight bridges first decreases and then increases. Increasing the span number enhances the stability of curved bridges, while its influence on straight bridges is more intricate. When examining the anti-overturning performance of curved bridges, the ROAM shows a similar pattern to the EFEM, while the SOAM displays comparable trends to the EFEM in both curved and straight bridges. However, the FOAM does not adequately capture the overall evolution of the anti-overturning performance in both types of bridges. For curved bridges, the ROAM has a minimum error of −12.2% to 20.5% compared to the EFEM, followed by the SOAM with an error of −20.7% to −32.4%. Conversely, the FOAM shows a significant error range of −77.6% to −98.7%, leading to a substantial underestimation of the anti-overturning capacity of curved bridges. For straight bridges, the ultimate vehicle weights obtained by the SOAM have the smallest error, compared to the EFEM results, with errors of −30.9% to 7.3%. The ultimate vehicle weight obtained by the FOAM is 26.1%, compared to 47.8% with the EFEM, indicating an underestimation of the anti-overturning capacity of straight bridges. Additionally, the ultimate vehicle weight obtained by the ROAM is 1.5 to 6.7 times that of the EFEM, suggesting an overestimation of the anti-overturning capacity of straight bridges.
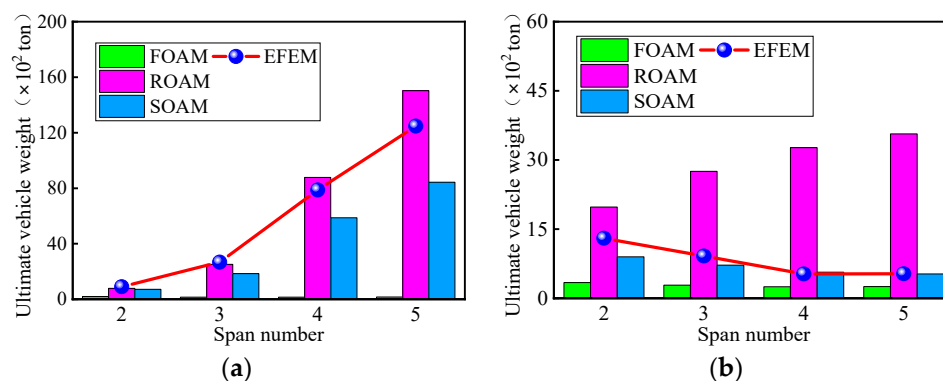
Figure 27. Ultimate vehicle weights for the bridges with various span numbers: (**a**) curved bridges; and (**b**) straight bridges.

Although the FOAM has been incorporated into the specification, it still exhibits a significant dispersion in the evaluation of anti-overturning between curved and straight bridges, severely underestimating the anti-overturning of curved bridges. This ultimately results in material wastage and a limit on freight traffic. In contrast, the SOAM, despite a maximum error of 38.8%, has significantly improved the accuracy of assessing anti-overturning capacity when compared to the FOAM and ROAM.

6. Conclusions

This study utilized a collapsed three-span continuous concrete girder bridge to replicate the overturning process caused by eccentric overloaded vehicles, validating the reliability of the numerical method. Furthermore, an EFEM model incorporating concrete creep was developed to assess its impact on long-term stability against overturning. The synthesis overturning axis method and related SOAM were proposed to improve the accuracy of the stability assessment for continuous girder bridges, especially curved ones. The conclusions drawn from this study are as follows:

(1) The analysis of eccentric vehicles crushing the accident bridges revealed that the bridge is briefly weightless after the large deformation of the girder rotates and then slips. During the girder's overturning, the vertical displacements on the non-overturned side and the overturned side become opposite and gradually increase, with the rotation angle following an 'S'-shaped development pattern. The simulation results align with the on-site wreckage, validating the numerical simulation's reliability in replicating the collapse process.

(2) As the vehicle weight increases, the sequence in which the bearings detach from the girder is as follows: A1-1 and A4-1, B2, B3, and A1-2 and A4-2. At the limit state of the overall overturning, the girder undergoes significant rotational deformation, reaching a rotation angle of 1.29 rad, where rigid rotation theory is not applicable. Limiting the rotation angle of the bearings or girder to within 0.02 rad fails to prevent the bearing disengagement but can prevent the overall overturning.

(3) Single-column pier bridges can be classified into curved, critical, and straight types based on the critical curvature radius. As the curvature radius increases, the ultimate vehicle weight of these bridges initially decreases and then increases, exhibiting minimal values in the critical bridge. Overall, straight bridges generally have smaller ultimate vehicle weights, indicating poorer overturning stability compared to curved bridges.

(4) Under the effects of creep and self-weight, the variations in the bearing reaction force for curved bridges and straight bridges are minimal, staying below 2%. The ultimate vehicle weight increases slightly with the increasing creep terminal coefficient for curved bridges and decreases for straight bridges. Despite these differences, all variations are within 2%. Therefore, the effect of concrete creep on the long-term overall overturning stability of single-column pier bridges can be neglected.

(5) Under the factors of the STMR, the SOAM results exhibit a similar trend to the EFEM in both curved and straight bridges. The error ranges of the ROAM, FOAM, and SOAM, compared with the EFEM, in terms of ultimate vehicle weight are −14.2% to 567.4%, −99.1% to −32.1%, and −38.8% to 33.9%, respectively. Despite the discrepancies, the SOAM demonstrates improvements in accuracy compared to the ROAM and SOAM in the overall anti-overturning assessment of single-column pier bridges.

(6) In this study, the effect of creep on the overall overturning stability of bridges was only analyzed with a specific creep mathematical model combined with numerical methods, and the conclusions need to be further verified by experiments. In addition, the relationship between the creep, bearing type and arrangement, and overturning stability of bridges should be further investigated.

Author Contributions: Conceptualization, Y.W.; Methodology, Y.W. and B.C.; Software, Y.W., J.T. and B.C.; Validation, Y.W. and D.Z.; Formal analysis, Y.W., J.T., D.Z., D.J. and B.C.; Investigation, Y.W. and D.Z.; Resources, Y.W., D.Z., D.J. and B.C.; Data curation, Y.W., J.T., D.Z., D.J. and B.C.; Writing—original draft, Y.W., J.T., D.J. and X.L.; Writing—review & editing, J.T., B.C. and X.L.; Visualization, D.Z., D.J. and X.L.; Supervision, J.T.; Project administration, J.T.; Funding acquisition, Y.W. All authors have read and agreed to the published version of the manuscript.

Conflicts of Interest: Author Dong Zheng was employed by the company Anhui Transport Consulting & Design Institute Co., Ltd. Authors Dayang Jing and Benzhen Cai were employed by Jinan Urban Construction Group Co., Ltd. Authors Xiaofeng Liu was employed by No.7 Geological Brigade, Shandong Provincial Bureau of Geology and Mineral Resources. The remaining authors declare that the research was conducted in the absence of any commercial or financial relationships that could be construed as a potential conflict of interest.

References

1. Xiong, W.; Cai, C.S.; Kong, B.; Ye, J. Overturning-collapse modeling and safety assessment for bridges supported by single-column piers. *J. Bridge Eng.* **2017**, *22*, 04017084. [CrossRef]
2. Deng, L.; Wang, W.; Yu, Y. State-of-the-art review on the causes and mechanisms of bridge collapse. *J. Perform. Constr. Facil.* **2016**, *30*, 04015005. [CrossRef]
3. Peng, W.B.; Dai, F.; Taciroglu, E. Research on mechanism of overturning failure for single-column pier bridge. In Proceedings of the 2014 International Conference on Computing in Civil and Building Engineering, Orlando, FL, USA, 23–25 June 2014; pp. 1747–1754.
4. Lee, K.; Andrawes, B.; Lim, J.; Kim, H.; Kang, Y. A study on overturning failure of horizontally curved single steel box girders. *Eng. Fail. Anal.* **2019**, *97*, 20–31. [CrossRef]
5. Liu, B.; Han, W.; Wang, T.; Feng, Y.; Wang, J.; Xu, K. Analytical method for overturning risk assessment of curved girder bridges with single-column piers under heavy-duty vehicles. *Structures* **2023**, *57*, 105084. [CrossRef]
6. Fan, Y.; Zhu, J.; Pei, J.; Li, Z.; Wu, Y. Analysis for Yangmingtan bridge collapse. *Eng. Fail. Anal.* **2015**, *56*, 20–27. [CrossRef]
7. Peng, W.B.; Zhao, H.; Dai, F.; Taciroglu, E. Analytical method for overturning limit analysis of single-column pier bridges. *J. Perform. Constr. Facil.* **2017**, *31*, 04017007. [CrossRef]
8. Peng, W.B.; Zhu, Z.X.; Chen, G.J.; Zhu, H.H. Research on overturning failure mode of beam bridges and applicability of calculation method. *China Civil Eng. J.* **2019**, *52*, 104–113.
9. Shi, X.; Cao, Z.; Ma, H.; Ruan, X. Failure analysis on a curved girder bridge collapse under eccentric heavy vehicles using explicit finite element method: Case study. *J. Bridge Eng.* **2018**, *23*, 05018001. [CrossRef]
10. Wang, B.J.; Zhao, H.; Zhang, H.; Peng, W.B.; Lu, C.Y. Lateral stability calculation theory and verification of single-column girder bridge. *China J. Highw. Transp.* **2017**, *30*, 93–100.
11. Song, T.; Deng, Q.; Li, G. Collapse mechanism and full-range analysis of overturning failure of continuous girder bridges. *Adv. Mater. Sci. Eng.* **2021**, *2021*, 1–14. [CrossRef]
12. Xu, H.; Li, Q.; Li, D.; Jiang, H.; Wang, T.; Gao, Q. Experimental and numerical investigation of the anti-overturning theory of single-column pier bridges. *Sustainability* **2023**, *15*, 1545. [CrossRef]
13. Song, G.; Che, D.; Li, M. Stability against overturning of curved continuous box-girder bridges with single column piers. *IOP Conf. Ser. Mater. Sci. Eng.* **2018**, *452*, 022105. [CrossRef]

14. Streit, W.; Mang, R. Uberschlägiger Kippsicherheitsnachweis für Stahlbeton-und Spannbetonbinder. *Bauingenieur* **1984**, *59*, 433–439.

15. Shi, X.; Zhou, Z.; Ma, H.; Emadi, S.; Cao, Z. Failure mechanism and design method for box girder bridge with interior hinged supports under eccentrically vertical loads. *Structures* **2023**, *48*, 438–449. [CrossRef]

16. Wang, J.F.; Xu, Z.Y.; Fan, X.L.; Lin, J.P. Thermal effects on curved steel box girder bridges and their countermeasures. *J. Perform. Constr. Facil.* **2017**, *31*, 04016091. [CrossRef]

17. Song, G.; Che, D.; Li, M. Overturning axis selection in curved box-girder bridges with single-column piers. *Math. Probl. Eng.* **2018**, *2018*, 1–9. [CrossRef]

18. Li, H.C.; Liu, X.D.; Feng, M. Overturning risk management of box-girder ramp bridge in operation period. *Highway* **2016**, *61*, 88–93.

19. Zhou, Y.J.; Wang, Y.L.; Zhao, Y.; Xue, Y.X.; Han, Z.Q. Review on research of anti-overturning of highway bridgers with single-column piers. *J. Traffic Transp. Eng.* **2022**, *22*, 46–66.

20. Ji, X.L.; Zhu, L.; Su, R.K.L.; Wang, G.M. Lateral overturning process and failure mechanism of curved steel-concrete composite box-girder bridges under specific overloading vehicles. *Structures* **2022**, *35*, 638–649. [CrossRef]

21. Xu, Z.; Lu, X.; Guan, H.; Lu, X.; Ren, A. Progressive-collapse simulation and critical region identification of a stone arch bridge. *J. Perform. Constr. Facil.* **2013**, *27*, 43–52. [CrossRef]

22. Wang, Y.L.; Zhou, Y.J.; Xue, Y.X.; Yao, C.W.; Wang, K.L. Failure analysis for overall overturning of concrete single-column pier bridges induced by temperature and overloaded vehicles. *Materials* **2024**, *17*, 2650. [CrossRef] [PubMed]

23. Deng, T.; Zhang, J.; Li, S.; Wang, Y. Anti-overturning stability coefficient of curved girder bridges considering seismic action. *J. Vibroeng.* **2019**, *21*, 710–725. [CrossRef]

24. Peng, K.K. Research on comprehensive evaluation method for antioverturning safety of bridges with bent-straight beam. *IOP Conf. Ser. Mater. Sci. Eng.* **2018**, *423*, 012012.

25. Li, S.; Yang, Y.; Pu, Q.; Yang, D.; Sun, B.; Li, X. Three-dimensional nonlinear creep and shrinkage effects of a long-span prestressed concrete box girder bridge. *Struct. Concr.* **2019**, *20*, 638–649. [CrossRef]

26. He, G.J.; Li, Y.Y.; Zou, Z.Q.; Duan, L.L. Effect of concrete creep on pre-camber of continuous rigid-frame bridge. *J. Cent. South Univ. Technol.* **2008**, *15*, 337–341. [CrossRef]

27. Zhan, Y.L.; Fan, Z.H.; Huang, Y.Y.; Zhang, Z.Q.; Shao, J.H.; An, J.W. Study on shrinkage and creep effect of steel truss-stiffened continuous rigid frame bridge considering variable temperature and relative humidity. *Structures* **2024**, *61*, 106120. [CrossRef]

28. Fan, X.; Zhou, H.; Liu, Y.F. Time-dependent reliability analysis of rc bridges considering shrinkage, creep, resistance degradation, and vehicle load flows. *Adv. Civ. Eng.* **2023**, *2023*, 1–14. [CrossRef]

29. Ma, J. Main bridge reinforcement of sanmenxia yellow river highway bridge. *Highway* **2004**, *6*, 62–64.

30. Bažant, Z.P.; Yu, Q.; Li, G.H. Excessive long-time deflections of prestressed box girders. I: Record-span bridge in Palau and other paradigms. *J. Struct. Eng.* **2012**, *138*, 676–686. [CrossRef]

31. People's Government of Wuxi. Investigation report on serious rollover accident of bridge deck on Xigang road of 312 national highway "10.10" in Wuxi. *Eng. Mech.* **2021**, *38*, 209.

32. Li, C.H.; Yang, L.B.; Fu, Z.H.; Liang, X.Y.; Peng, W.B.; Jia, X.J. Forensic analysis of the wuxi 312 viaduct overturning collapse. *Eng. Mech.* **2021**, *38*, 203–211.

33. *JT/T 391-2019 (MTPRC 2019)*; Pot bearings for Highway Bridges. Ministry of Transport of the People's Republic of China: Beijing, China, 2019.

34. Bazant, Z.P.; Wittmann, F.H. *Creep and Shrinkage in Concrete Structures*; Wiley: New York, NY, USA, 1982; pp. 163–181.

35. Tyler, R.G. Creep, shrinkage and elastic strain in concrete bridges in the United Kingdom, 1963–1971. *Mag. Concr. Res.* **1976**, *28*, 55–84. [CrossRef]

36. Xiang, H.F.; Zhu, L.D. *Advanced Theory of Bridge Structures*; Communications Press Co., Ltd.: Beijing, China, 2013; pp. 113–120.

37. Yang, I.H. Probabilistic analysis of creep and shrinkage effects in PSC box girder bridges. *KSCE J. Civ. Eng.* **2003**, *7*, 275–284. [CrossRef]

38. Williams, M.; Menon, D.; Prasad, A.M. Creep and shrinkage in prestressed concrete beams: An experimental study. *Struct. Concr.* **2024**, *2024*, 1–24. [CrossRef]

39. *No. 124/125E*; Model Code for Concrete Structures. CEB Bulletin d'Information: Paris, France, 1978.

40. *No. 213/214*; CEB-FIP Model Code 1990. CEB Bulletin d'Information: Lausanne, Switzerland, 1993.

41. Kolínský, V.; Vítek, J.L. Verification of numerical creep and shrinkage models in an arch bridge analysis. *Struct. Concr.* **2019**, *20*, 2030–2041. [CrossRef]

42. Tong, T.; Liu, Z.; Zhang, J.; Yu, Q. Long-term performance of prestressed concrete bridges under the intertwined effects of concrete damage, static creep and traffic-induced cyclic creep. *Eng. Struct.* **2016**, *127*, 510–524. [CrossRef]

43. Whirley, R.G.; Henshall, G.A. Creep deformation structural analysis using an efficient numerical algorithm. *Int. J. Numer. Meth. Eng.* **1992**, *35*, 1427–1442. [CrossRef]

44. Zhao, Y.; Wang, Z.W.; Yao, T.Y.; Zhou, Y.J. Refinement analysis of pc beam creep effect under variable load considering creep recovery. *China J. Highw. Transp.* **2023**, *36*, 345–356.

45. *JTG D60-2015 (MTPRC 2004)*; General Specifications for Design of Highway Bridges and Culverts. Standards Press: Beijing, China, 2015.

46. Zhuang, D.; Xiao, R.; Jia, L.; Sun, B. Failure analysis for overall stability against sliding and overturning of a girder bridge. *Eng. Fail. Anal.* **2020**, *109*, 104271. [CrossRef]
47. *AASHTO 2012*; AASHTO LRFD Bridge Design Specifications. American Association of State Highway and Transportation Officials: Washington, DC, USA, 2012.
48. *JTG/T 3362-2018 (MTPRC 2018)*; Specifications for Design of Highway Reinforced Concrete and Prestressed Concrete Bridges and Culverts. Communications Press Co., Ltd.: Beijing, China, 2018.
49. *TB100023-2005 (MTPRC 2005)*; Code for Design on Reinforced and Prestressed Concrete Structures of Railway Bridges and Culverts. Ministry of Railways of the People's Republic of China: Beijing, China, 2005.
50. *JRA 2012*; Specifications for Road and Bridge Designs. Japan Road Association: Tokyo, Japan, 2012.